The Astrophysical Journal Letters, 893:L25 (9pp), 2020 April 10 https://doi.org/10.3847/2041-8213/ab846e

In Situ Measurement of Curvature of Magnetic Field in Turbulent Space Plasmas: A Statistical Study

Riddhi Bandyopadhyay[1,2], Yan Yang[3,4], William H. Matthaeus[1,2], Alexandros Chasapis[5], Tulasi N. Parashar[1,2,11], Christopher T. Russell[6], Robert J. Strangeway[6], Roy B. Torbert[7], Barbara L. Giles[8], Daniel J. Gershman[8], Craig J. Pollock[9], Thomas E. Moore[8], and James L. Burch[10]

[1] Department of Physics and Astronomy, University of Delaware, Newark, DE 19716, USA; riddhib@udel.edu
[2] Bartol Research Institute, University of Delaware, Newark, DE 19716, USA
[3] Southern University of Science and Technology, Shenzhen, Guangdong 518055, People's Republic of China
[4] University of Science and Technology of China, Hefei, Anhui 230026, People's Republic of China
[5] Laboratory for Atmospheric and Space Physics, University of Colorado Boulder, Boulder, CO, USA
[6] University of California, Los Angeles, CA 90095-1567, USA
[7] University of New Hampshire, Durham, NH 03824, USA
[8] NASA Goddard Space Flight Center, Greenbelt, MD 20771, USA
[9] Denali Scientific, Fairbanks, AK 99709, USA
[10] Southwest Research Institute, San Antonio, TX 78238-5166, USA
Received 2020 January 25; revised 2020 March 27; accepted 2020 March 29; published 2020 April 14

Abstract

Using in situ data, accumulated in the turbulent magnetosheath by the Magnetospheric Multiscale Mission, we report a statistical study of magnetic field curvature and discuss its role in the turbulent space plasmas. Consistent with previous simulation results, the probability distribution function of the curvature is shown to have distinct power-law tails for both high and low value limits. We find that the magnetic-field-line curvature is intermittently distributed in space. High curvature values reside near weak magnetic-field regions, while low curvature values are correlated with small magnitude of the force acting normal to the field lines. A simple statistical treatment provides an explanation for the observed curvature distribution. This novel statistical characterization of magnetic curvature in space plasma provides a starting point for assessing, in a turbulence context, the applicability and impact of particle energization processes, such as curvature drift, that rely on this fundamental quantity.

Unified Astronomy Thesaurus concepts: Space plasmas (1544); Plasma physics (2089); Magnetohydrodynamics (1964)

1. Introduction

The curvature of the magnetic field enters in numerous important ways in electrodynamics (Petschek 1964) and plasma physics (Boozer 2005), representing one of the principal ways that magnetic fields interact with matter. Curvature plays a key role in magnetic reconnection (Petschek 1964), stability of magnetic confinement (Dobrott et al. 1977), in magnetospheric physics and space physics (Hameiri et al. 1991), and in particle heating and acceleration (Pesses et al. 1981; Jokipii 1982; Dahlin et al. 2014). Usually, curvature is studied with regard to specific magnetic configurations. For example, stability with respect to ballooning modes requires favorable curvature that is antiparallel to the pressure gradients (Boozer 2005). Similarly, the large curvature of field lines in reconnection exhausts gives rise to relaxation toward a less stressed state, leading to electron energization by curvature drift acceleration (Dahlin et al. 2014). Magnetic-field curvature has been useful for detecting helical field configuration of flux ropes from in situ measurements (Slavin et al. 2003; Shen et al. 2007; Sun et al. 2019).

Recently, the curvature of magnetic field lines has been studied in the magnetohydrodynamic (MHD) model of plasma turbulence (Yang et al. 2019). In the case of turbulence, it is impractical to study curvature of individual field lines and one may resort to a statistical approach, as is typical in studies of turbulence (Monin & Yaglom 1971). In these simulations, one finds interesting properties such as a distribution of curvature that exhibits two power-law regimes, and a systematic anticorrelation of curvature with magnetic field strength, for low values of magnetic field strength. Here, we extend this statistical examination of magnetic curvature by analysis of in situ satellite observations in the terrestrial magnetosheath. We employ Magnetospheric Multiscale (MMS) data that reveal distributions and correlations that are consistent with, and in fact very similar to, those observed in the MHD simulations (Yang et al. 2019). These results confirm the theoretical model given in Yang et al. (2019), opening the door to new applications such as curvature drift acceleration in turbulence as well as the possible role of local explosive instabilities in turbulence.

The outline of the Letter is as follows: In Section 2, we discuss the theoretical derivation and approximations. In Section 3, we apply the theoretical constructs to MMS data and present the results. We discuss the importance of the results and conclude in Section 4. In Appendices A and B, we justify the assumptions made in Section 2. Appendix C shows the results presented in Section 3 for a different MMS interval.

2. Theory and Method

The curvature κ of magnetic field $\boldsymbol{B}$ is defined as

$$\kappa = |\boldsymbol{b} \cdot \nabla \boldsymbol{b}|, \quad (1)$$

[11] Now at: School of Chemical and Physical Sciences, Victoria University of Wellington, Kelburn, Wellington 6012, NZ.

where $\boldsymbol{b} = \boldsymbol{B}/B$ and $B = |\boldsymbol{B}|$. It can be expressed also in the form

$$\kappa = \frac{|\boldsymbol{b} \times (\boldsymbol{B} \cdot \boldsymbol{\nabla B})|}{B^2} = \frac{f_n}{B^2}, \quad (2)$$

where $f_n = |\boldsymbol{b} \times (\boldsymbol{B} \cdot \boldsymbol{\nabla B})|$ is the magnitude of the tension force (per unit volume) acting normal to the field lines. In the curvilinear coordinate attached to a field line, traced by a trajectory $\boldsymbol{\gamma}(s)$, the scalar s is a coordinate along the field line, while $\boldsymbol{e}_t = \frac{d\gamma}{ds}\Big/\left|\frac{d\gamma}{ds}\right| = \boldsymbol{b}$ and $\boldsymbol{e}_n = \frac{d^2\gamma}{ds^2}\Big/\left|\frac{d^2\gamma}{ds^2}\right|$ are the unit vectors in the tangential and normal directions along the field line, respectively. Then

$$\boldsymbol{B} \cdot \boldsymbol{\nabla B} = (B\boldsymbol{e}_t) \cdot \boldsymbol{\nabla}(B\boldsymbol{e}_t) = B\frac{\partial(B\boldsymbol{e}_t)}{\partial s} = B\frac{\partial B}{\partial s}\boldsymbol{e}_t - \kappa B^2 \boldsymbol{e}_n. \quad (3)$$

Equation (2) follows directly from Equation (3).

It is shown in the following section that high curvature values are well associated with weak magnetic field. In contrast, low curvature values mainly result from small normal force, more so than from large values of magnetic field. These findings point the way to explain the power-law tails in the curvature distribution in both the high value range and the low value range, reasoning as follows Yang et al. (2019).

First, let us consider the low value range. Noting that the normal force is two-dimensional, we write its Cartesian components as f_1 and f_2, and then assume that these are independent random variables and their probability distribution function (PDFs) for small values obey the Gaussian distribution. Then the PDFs of f_1 and f_2 at small values may be written as

$$P_{f_1}(f) = P_{f_2}(f) = \frac{1}{\sqrt{2\pi\sigma_1^2}} e^{-\frac{f^2}{2\sigma_1^2}}, \quad (4)$$

where f denotes the vale of either f_1 or f_2 at the point of interest, and σ_1^2 is the variance. The quantity $f_n^2/\sigma_1^2 = (f_1^2 + f_2^2)/\sigma_1^2$ should then be distributed according to the chi-squared distribution with 2 degrees of freedom. The corresponding PDF of f_n at small values (i.e., $f_n \to 0$) is

$$P_{f_n}(f) = \frac{f}{\sigma_1^2} e^{-\frac{f^2}{2\sigma_1^2}}. \quad (5)$$

Here, f represents the value of the variable f_n. See Appendix A where a slightly more general, but equivalent, development is given. Since $\kappa = f_n B^{-2}$ and low curvature κ is determined by the scaling behavior of small normal force f_n, the PDF of curvature as $\kappa \to 0$ can be written as

$$P_\kappa(\kappa') = B^2 P_{f_n}(\kappa' B^2) = \frac{B^4 \kappa'}{\sigma_1^2} e^{-\frac{B^4 \kappa'^2}{2\sigma_1^2}}. \quad (6)$$

Here, κ' is the value of the variable κ. Let us assume that B is finite in this limit, which could be replaced with $B_{\rm rms}$ in Equation (6). Then the Taylor series of the PDF around $\kappa' = 0$ is

$$\frac{B^4}{\sigma_1^2}\left(\kappa' - \frac{B^4}{2\sigma_1^2}\kappa'^3 + \cdots\right). \quad (7)$$

The higher-degree terms are much smaller as $\kappa' \to 0$, so we retain only the lowest-order term, and obtain

$$P_{\kappa \to 0}(\kappa') \sim \kappa'^1. \quad (8)$$

In a similar way, we can explain the power-law tail of the PDF for high curvature values. In isotropic turbulence, we suppose that x, y, and z components of magnetic fluctuations are independent Gaussian random variables. Then

$$B_x,\ B_y,\ B_z \sim \mathcal{N}(0, \sigma_2^2), \quad (9)$$

where $\mathcal{N}(0, \sigma_2^2)$ denotes the normal distribution with mean 0 and variance σ_2^2. In real systems, the magnetic fields are never fully isotropic, so we eliminate the average from each component and work with the fluctuations. Note that, in a turbulent system, the *increments* of the magnetic field are intermittently distributed with super-Gaussian tails (Matthaeus et al. 2015), but the fluctuation components themselves are rather well described by Gaussian distribution (Batchelor 1951; Padhye et al. 2001; also see Appendix B). The quantity $B^2/\sigma_2^2 = (B_x^2 + B_y^2 + B_z^2)/\sigma_2^2$, therefore, follows the chi-squared distribution with 3 degrees of freedom. The corresponding PDF of B^2 is

$$P_{B^2}(b') = \frac{\sqrt{b'}}{(2\sigma_2^2)^{3/2}\,\Gamma(3/2)} e^{-\frac{b'}{2\sigma_2^2}}, \quad (10)$$

where, b' represents the value of B^2 at the point of interest, and Γ is the gamma function. Since $\kappa = f_n B^{-2}$ and high curvature κ is determined by the scaling behavior of weak magnetic field B^2, the PDF of curvature as $\kappa \to \infty$ can be written as

$$P_\kappa(\kappa') = \frac{f_n}{\kappa'^2} P_{B^2}\left(\frac{f_n}{\kappa'}\right) = \frac{f_n^{3/2}\ \kappa'^{-5/2}}{(2\sigma_2^2)^{3/2}\,\Gamma(3/2)} e^{-\frac{f_n}{2\sigma_2^2}}. \quad (11)$$

Again, κ' is the value of the variable κ. In analogy to the prior case, we assume that f_n remains finite in this limit, and replace the associated value with the average $\langle f_n \rangle$ in Equation (11). Then the Taylor series for the PDF about $1/\kappa' = 0$ becomes

$$\frac{f_n^{3/2}}{(2\sigma_2^2)^{3/2}\,\Gamma(3/2)}\left(\kappa'^{-5/2} - \frac{f_n}{2\sigma_2^2}\kappa'^{-7/2} + \cdots\right). \quad (12)$$

It follows that in the limit as $\kappa' \to \infty$, i.e., $1/\kappa' \to 0$, the curvature PDF scales as

$$P_{\kappa \to \infty}(\kappa') \sim \kappa'^{-5/2}. \quad (13)$$

Previously (Yang et al. 2019), the above reasoning was found to explain the behavior of the distributions of curvature in three-dimensional, isotropic, MHD simulations. We now extend this inquiry to the case of a naturally occurring space plasma, the turbulent magnetosheath.

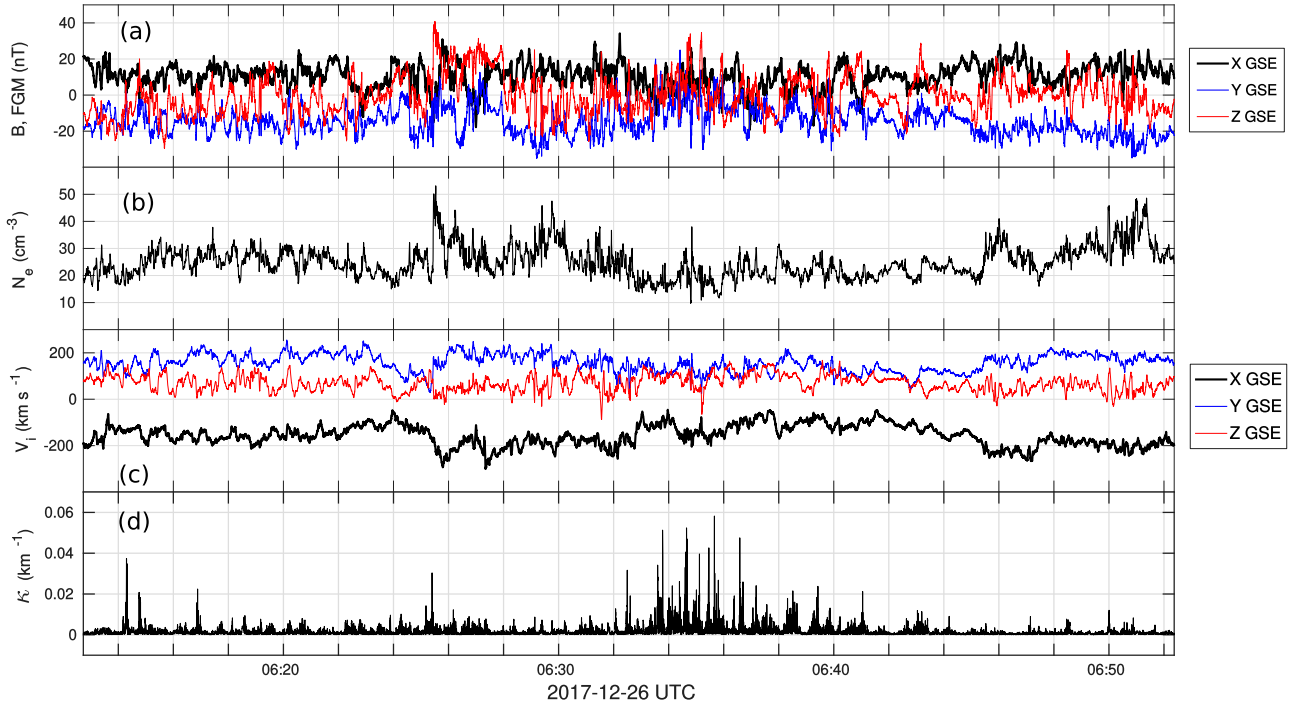

Figure 1. Overview of the MMS observations in the turbulent magnetosheath selected for this study. The data shown are from the FGM and FPI instruments on board the MMS1 spacecraft. Panel (a) shows the magnetic field measurements in GSE coordinates. Panel (b) shows the electron density. Panel (c) shows the ion velocity in GSE coordinates. Panel (d) shows the curvature calculated (approximately using a curlometer-like method) from the magnetic field (see Equation (1)).

Below, we use four-spacecraft linear estimates of gradient, similar to the "curlometer" method (Dunlop et al. 1988; Paschmann & Daly 1998) to calculate $\boldsymbol{\nabla b}$. Then a dot product with $\boldsymbol{b}$ yields the curvature $\kappa = |\boldsymbol{b} \cdot \boldsymbol{\nabla b}|$. In Section 3, we use this approach to analyze the statistical properties of the curvature field using MMS observations, including the accuracy of the above scaling arguments.

3. MMS Observations

MMS consists of four identical spacecraft orbiting the Earth, for the chosen period, in a tetrahedral formation with small (∼10 km) separation. The four MMS spacecraft sample the near-Earth plasma including the magnetosheath (Burch et al. 2016). The Fast Plasma Investigation (FPI; Pollock et al. 2016) instrument calculates the proton and electron three-dimensional velocity distribution functions (VDFs) and the Flux-Gate Magnetometer (FGM; Russell et al. 2016) measures the vector magnetic field.

In burst mode, the Dual Ion Spectrometer (DIS) and the Dual Electron Spectrometer (DES) in FPI/MMS measure the ion and electron VDF at a cadence of 150 ms and 30 ms, respectively. Plasma moments are calculated from each VDF at the corresponding time resolution. The time resolution of the FGM magnetic field is 128 Hz in burst mode.

To cover a large statistical sample of the turbulent plasma in the magnetosheath, here we focus on one long MMS burst-mode interval between 06:12:43 and 06:52:23 UTC on 2017 December 26. A time-series plot of the selected interval is shown in Figure 1. The FGM magnetic field components, in the geocentric solar ecliptic (GSE) coordinate system (Franz & Harper 2002), are shown in panel (a). The magnetic field components exhibit large-amplitude fluctuations that are typical for magnetosheath plasma. The electron density estimates are often more accurate than the ion density in the magnetosheath due to higher thermal speed. Panel (b) plots the electron density, obtained from the FPI/DES distributions. The three GSE components of the ion velocity components, measured by FPI/DIS, are plotted in panel (c). The final panel (d) shows the time series of the curvature field, derived from the magnetic field by a finite difference curlometer-like method (see Section 2). The curvature values are observed to be highly intermittent with thin "spikes" distributed during the whole interval that suggest the presence of sheet-like structures.

Table 1
Description of MMS Data Set from 06:12:43 to 06:52:23 UTC on 2017 December 26

MMS Position $(X, Y)_{GSE}$	$\lvert\langle \boldsymbol{B} \rangle\rvert$ (nT)	$B_{rms}/\lvert\langle \boldsymbol{B} \rangle\rvert$	L (km)	d_i (km)	β_p
(10 R_e, 9 R_e)	17.9	0.8	27	47	4.4

Note. The quantities are defined in the text.

Several important plasma parameters of the selected MMS interval are reported in Table 1, including the locations of the MMS spacecraft in the GSE coordinate system, in units of Earth radius (R_e) during the interval, mean magnetic field ($\lvert\langle \boldsymbol{B} \rangle\rvert$), ratio of rms fluctuation amplitude of the magnetic field (B_{rms}) to the mean magnetic field, average spacecraft separation L, ion-inertial length (d_i), and the average plasma beta (β_p). The rms fluctuation amplitude is defined as $B_{rms} = \sqrt{\langle |\boldsymbol{B}(t) - \langle \boldsymbol{B} \rangle|^2 \rangle}$, which has a value of 14 nT here. The spacecraft separations are much smaller than the ion-inertial length. However, using the curlometer method in the determination of gradients, there are some errors associated that affect the estimation of f_n and κ. Following Shen et al. (2003, 2007), the fractional error in the curvature values

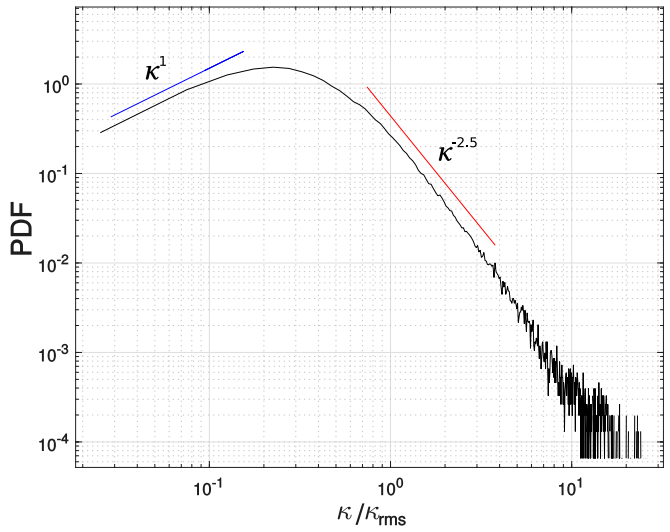

Figure 2. PDF of the magnetic field curvature κ normalized to its rms value κ_{rms}, computed from the 40 minute MMS data set shown in Figure 1.

can be estimated roughly as

$$\frac{\Delta\kappa}{\kappa} \sim \mathcal{O}(L\kappa), \tag{14}$$

where L is the spacecraft separation. For the present interval, we may use $L \sim 10$ km. From Figure 1, the maximum of the curvature values reaches about $\kappa \sim 0.5\,\mathrm{km}^{-1}$. Therefore, the fractional error in curvature remains within ~0.5. Further, by comparing the FPI current and curlometer current, several studies have found that the MMS curlometer usually works well in the magnetosheath (e.g., Gershman et al. 2018; Stawarz et al. 2019). Therefore, the results presented below are expected to be reliable.

The main quantitative observational result of this study is contained in Figure 2, which shows the PDFs of the curvature for the ≈40 minute magnetosheath interval of MMS data described in Table 1 and shown in Figure 1. Many prior studies (e.g., Shen et al. 2003, 2007; Slavin et al. 2003; Rong et al. 2011; Akhavan-Tafti et al. 2019; Sun et al. 2019) have explored curvature of the magnetic field in the magnetosphere for individual events or collection of structures, but as far as we are aware, this is the first detailed analysis of *statistics* of magnetic-field curvature in turbulent space plasmas using observational data.

The PDF shown in Figure 2 exhibits two distinct power-law regimes: at low values of the curvature field, its distribution scales roughly as κ^{+1}, while at high curvature values the distribution behaves as $\kappa^{-2.5}$. This is remarkably similar to the empirical and theoretical findings of Yang et al. (2019).

To further clarify the statistics of the magnetic curvature, Figure 3 shows the joint probability distributions of curvature and squared magnetic field magnitude, and curvature and normal force. The relationship between high curvature and regions of weak magnetic field is corroborated by the former. In Figure 2, the power-law regimes are separated at $\kappa/\kappa_{rms} \lessapprox 0.1$ and $\kappa/\kappa_{rms} \gtrapprox 1$. From the left panel of Figure 3, the curvature and magnetic field are rather well associated for $\kappa/\kappa_{rms} \gtrapprox 1$, and the association begins to weaken at $\kappa/\kappa_{rms} \lessapprox 0.1$. The Pearson-$r$ coefficient between κ/κ_{rms} and $(B/B_{rms})^2$ for $\kappa/\kappa_{rms} \geqslant 0.9$ has a magnitude of 0.53, and it is 0.005 for $\kappa/\kappa_{rms} \leqslant 0.15$. This is consistent with the intuition that weak magnetic fields are easier to bend, and leads to the above-described $\kappa^{-2.5}$ curvature distribution in the weak magnetic field regime.

Similarly, the positive correlation between curvature and normal force per unit volume at low curvature is shown in Figure 3 (right panel). Again, at small curvature values, κ and f_n are well correlated with a Pearson-r coefficient value of 0.12 for $\kappa/\kappa_{rms} \leqslant 0.15$, However, at a high curvature value the association is not so clear, resulting in a Pearson-r value of 0.02 for $\kappa/\kappa_{rms} \geqslant 0.9$. This supports the reasoning that leads to the κ^{+1} behavior of the κ distribution at the small values of curvature. These quantifications are summarized in Table 2.

The interval shown in Figure 1 is selected for no special reason other than its long duration and the preliminary observation that it exhibits well-developed turbulence properties (Parashar et al. 2018). The same analyses on other turbulent magnetosheath intervals produce similar results (see Appendix C and Figure C1).

As a final, direct observational diagnostic, in the two panels in Figure 4 we show small samples of the time series of curvature and magnetic field (top panel) and curvature and the normal force (bottom panel) to illustrate how large (small) curvature regions are often localized in regions of low magnetic field strength (low normal force strength).

Indeed, from the top panel of Figure 4 one observes several *peaks* in curvature values that are contemporaneous with sharp drops in the magnetic field strength. Similarly, from the bottom panel, strong *dips* in the curvature are accompanied by dips in the normal force values. For clarity, only small subintervals of the whole magnetosheath interval are shown. We note that only curvature large enough, say, $\kappa/\kappa_{rms} \gtrapprox 1$ (i.e., the right power-law regime in Figure 2), is associated with small B, and only curvature small enough, say, $\kappa/\kappa_{rms} \lessapprox 0.1$ (i.e., the left power-law regime in Figure 2), is associated with small f_n. This behavior is also consistent with the trends seen in Figure 3 and Table 2.

4. Discussion

Employing the unique capabilities of the MMS mission, we have studied the statistical properties of the curvature of the magnetic field measured in the terrestrial magnetosheath by the FGM instrument on board each of the four spacecraft. The data set employed is a long, 40 minute duration, burst-mode interval in the terrestrial magnetosheath. This determination of the statistical character of the magnetic curvature is the first of its kind in a space plasma, as far as we are aware.

We find two power-law regimes in the distribution of values of curvature: a κ^{+1} regime at low κ, and a $\kappa^{-2.5}$ regime at large κ. We also find an anticorrelation of curvature and magnetic field strength at low magnetic field strength, and a positive correlation of curvature and normal force per unit volume at small values of the force. All of these results are consistent with the findings of Yang et al. (2019), based on MHD simulations. What is more remarkable is the degree of quantitative agreement of the present observations with the MHD results. The simple theory outlined here clearly is adequate to explain the two power-law ranges in the curvature that are seen in both simulations and observations.

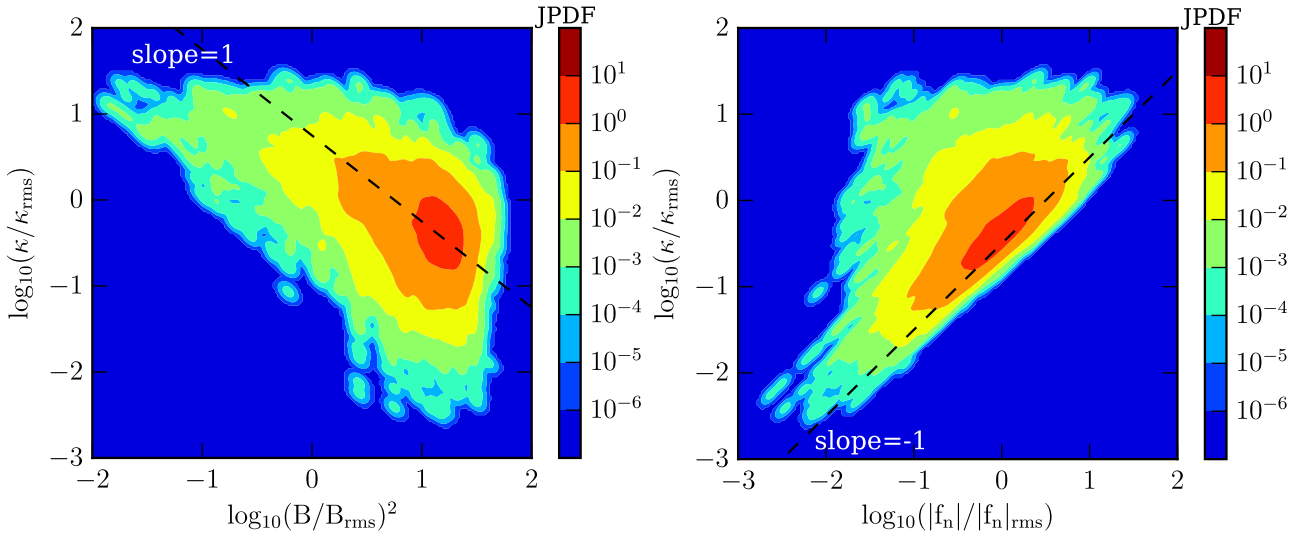

Figure 3. Joint PDFs of curvature κ and (left panel) the square of magnetic field magnitude B^2 and (right panel) the magnitude of the force $|f_n|$ acting normal to the field lines. All quantities are normalized to their respective rms values. Dashed lines with slope of 1 and −1 are shown for reference.

Table 2
Pearson's-r Coefficient between Curvature and Magnetic Field Strength, and Normal Force for Low and High Curvature Ranges

		Range	
		$\kappa/\kappa_{\rm rms} \leqslant 0.15$	$\kappa/\kappa_{\rm rms} \geqslant 0.9$
Variables	$\kappa/\kappa_{\rm rms}$, $(B/B_{\rm rms})^2$	$r = 0.005$	$r = -0.53$
	$\kappa/\kappa_{\rm rms}$, $\lvert f_n\rvert/\lvert f_n\rvert_{\rm rms}$	$r = 0.12$	$r = 0.02$

It is interesting to note that the kind of distribution we find for curvature (Figure 2) has been studied in applied mathematics and is known as a "double-Pareto" distribution (Reed 2001; Reed & Hughes 2002; Reed & Jorgensen 2004; Fang et al. 2012), generalizing the standard nomenclature of the Pareto distribution for a range of scale-invariant power-law behavior (Mitzenmacher 2004). This type of distribution generally indicates a multiplicative process. However, if such a process is uninhibited it leads to a lognormal distribution. When a physical effect, such as the inner scale of turbulence, or the particle gyromotion changes the physics and limits the process, it becomes a double-Pareto. The mathematics of such processes may provide fruitful directions for additional study of the nature of magnetic field curvature and its effects on particle acceleration.

One possibility that presents itself is that these results may be applicable to turbulent magnetic fields in other venues including other heliospheric environments and perhaps in astrophysical contexts as well. We note that, in order to derive the power-law scalings, Equations (8) and (13), we assume that the magnetic field components are isotropically distributed. Real systems are never perfectly isotropic at any length scale, but the magnetosheath conditions are rather close to isotropy with a weak DC field (see Figure 1 and Table 1). Extending the present study to other plasma systems, e.g., solar wind, magnetotail, magnetosphere, etc., would require appropriate modification to the derivation, although the basic arguments are expected to remain unchanged. Independent confirmation from other simulations, laboratory experiments, as well as other observations, if available, is called for. To the extent that these

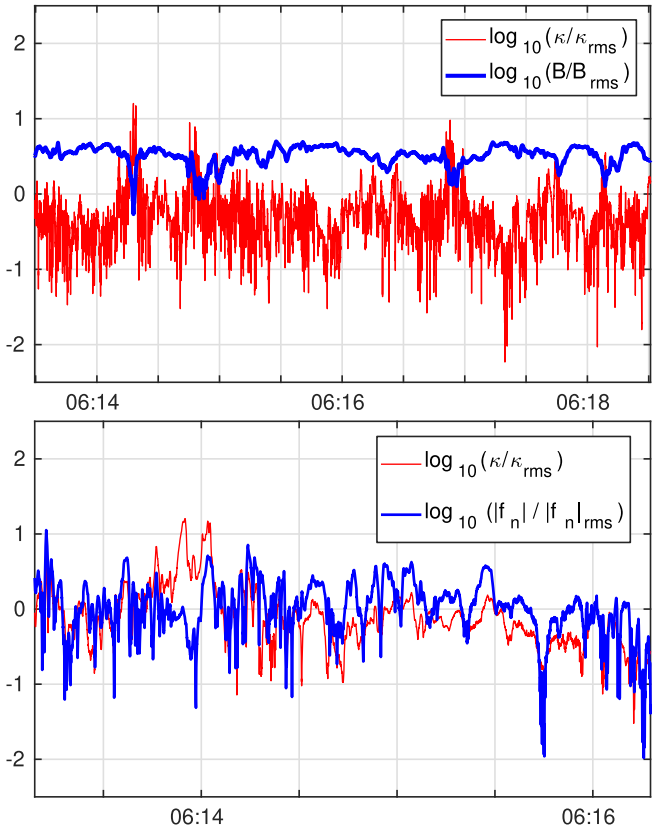

Figure 4. Time series of the curvature field, in the thin red line, superposed on the magnetic-field magnitude (top panel) and the magnitude of the normal force (bottom panel), in the broad blue line, and for a small subinterval of the whole magnetosheath interval.

results are robust, at least one major theoretical application is suggested. Specifically, curvature drift acceleration theory (e.g., Hoshino et al. 2001; Dahlin et al. 2014; Guo et al. 2015) has apparently been very successful in explaining electron energization in individual magnetic reconnection events. Since this theory depends explicitly on κ, one would expect that an immediate extension based on the present results

would be to include a statistical distribution of curvature values, to develop a curvature drift energization mechanism appropriate to magnetized plasma turbulence.

This research was partially supported by NASA under the Magnetospheric Multiscale Mission (MMS) Theory and Modeling program grant NNX14AC39G and by NASA Heliospheric Supporting Research Grant NNX17AB79G. We would like to acknowledge the assistance of the MMS instrument teams, especially FPI and FIELDS, in preparing the data, as well as the work done by the MMS Science Data Center (SDC). The data used in this work are Level 2 FIELDS data products, in cooperation with the instrument teams and in accordance with their guidelines. All MMS data used in this study are publicly available at the MMS Science Data Center (https://lasp.colorado.edu/MMS/sdc/public/). The Interplanetary Magnetic Field (IMF) data, measured by the Wind spacecraft, are used to determine the angle between the shock normal and the IMF in Appendix B. The IMF, shifted to Earth's bow-shock nose, can be found at https://omniweb.gsfc.nasa.gov/. The authors thank the Wind team for the Wind magnetic field data.

Appendix A
Distribution of Normal Force at Small Values

In deriving the scaling properties of curvature, κ, at low-κ values (Equation (8)), we assume that the normal force components f_1 and f_2 are independent Gaussian variables for small values. However, the only result that is actually used in the subsequent development is Equation (5) which is the distribution of the values of the *magnitude* of the normal force, f_n. The exact form of the distributions of f_1 and f_2, therefore, is not a salient point. Rather, if f_n follows a chi-squared distribution with 2 degrees of freedom (Equation (5)) for small values of f_n, that would support the subsequent development of the theory. Figure A1 shows the distribution of f_n and compares it with Equation (5) for the interval analyzed in the main text. It is evident that the small values of normal force are well described by Equation (5).

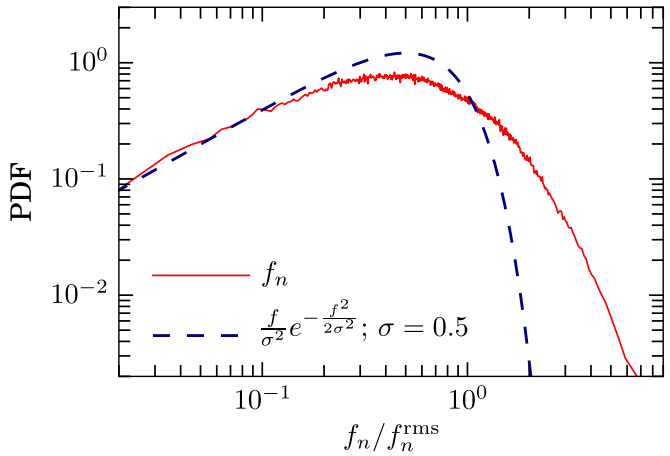

Figure A1. PDFs of the value of the normal force f_n as computed from MMS data analyzed using the 40 minute interval analyzed in this Letter.

Appendix B
Distribution of Magnetic-field Components in the Magnetosheath Plasma

In deriving the scaling properties of curvature, κ, at high-κ values (Equation (13)), we assume that the probability distribution of magnetic-field components is approximately Gaussian, e.g., in Equation (9). Although established in the pristine solar wind at 1 au (Padhye et al. 2001), and expected in general for primitive variables in turbulence (Batchelor 1951), the Gaussianity of the turbulent fluctuations in the magnetosheath has not been previously quantified, as far as we are aware (although see Whang 1977). To justify this approximation, here we examine the PDFs of the fluctuations of the magnetic field components using an analysis of several MMS data sets. Functional fits as well as moment comparisons (kurtoses) are used in drawing conclusions concerning the degree of non-Gaussianity.

To begin, we analyze the main 40 minute data interval analyzed in the text, shown in Figure 1 and described in Table 1. The data from each spacecraft are rank-ordered into 100 bins of variable width such that each bin has an equal number of data points. For each component, data from all four spacecraft are collected together to increase the statistical weight. The density of points in each bin provides an approximation to the PDFs, This procedure is carried out for the fluctuating magnetic-field components, and these empirically determined PDFs are shown in Figure B1. The solid curves are the corresponding Gaussian PDFs with zero mean and a variance equal to that computed from the data. The goodness of fit is measured by χ^2, defined as

$$\chi^2 = \frac{\sum_i [f(a_i) - g(a_i)]^2\ \Delta a_i}{\sum_i [f(a_i)]^2\ \Delta a_i}, \tag{B1}$$

where $f(a_i)$ is the observed PDF of any magnetic-field component, and $g(a_i)$ is the corresponding Gaussian distribution. For a perfect agreement ($f = g$), $\chi^2 = 0$; a small value of χ^2 indicates satisfactory fitness.

Quantitative results for the main 40 minute MMS interval are shown in the first row of entries of Table B1. As figures of merit, the values of the parameter χ^2 are listed along with values of the kurtosis for each component. While the goodness of the Gaussian representation is measured by χ^2, the closeness of the PDFs to Gaussian distributions can be also be quantified by the kurtosis. The kurtosis for a Gaussian distribution is 3; a kurtosis value greater (less) than 3 represents a super-(sub-) Gaussian distribution (Matthaeus et al. 2015). The closeness of the PDFs of the magnetic-field components to Gaussian is clear from Figure B1 and from the values of χ^2 and kurtoses listed in Table B1. On deriving the power law of the curvature PDF at large values, we also neglect the differences among B_x, B_y, B_z distributions, i.e., the variances of the three components are the same in Equation (9). For the 40 minute MMS interval we have $\sigma_{B_x} = 7$, $\sigma_{B_y} = 8$, $\sigma_{B_x} = 10$, which can also be seen from the the width of the three distributions shown in Figure B1.

To draw a more proper conclusion, we further analyze a few other turbulent magnetosheath intervals. Note that for good statistical weight, long intervals are required. Therefore, we select magnetosheath intervals of at least a few minutes duration and with no prominent discontinuity. All the selected intervals have a large fluctuation amplitude with $B_{\rm rms}/|\langle \boldsymbol{B} \rangle| \gtrsim 1$, and the

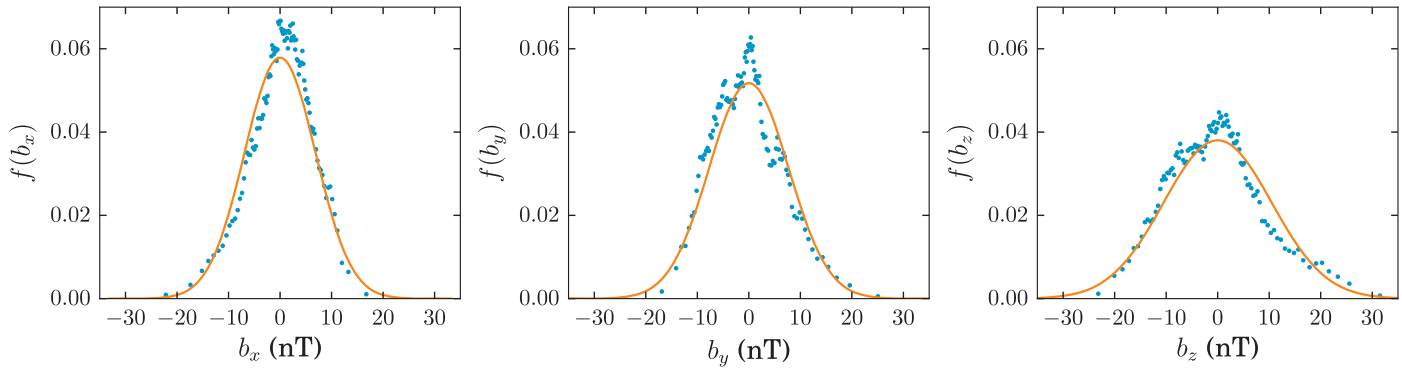

Figure B1. PDFs of fluctuations of the magnetic field as computed from MMS data analyzed in this Letter. *X*, *Y*, and *Z* components are shown in the left, middle, and right panels. The dots represent centers of the binned data, and the solid line shows the reference Gaussian. Each of the 100 bins contains 15,373 measurements.

Table B1
Kurtoses and χ^2 Values for the Magnetic Field Components Measured by MMS in the Magnetosheath

Interval	MMS Position $(X, Y)_{GSE}$	Parameter	b_x	b_y	b_z	$B_{rms}/\lvert\langle \boldsymbol{B}\rangle\rvert$	Shock Type
2017 Dec 26, 06:12:43–06:52:23	(10 R_e, 9 R_e)	χ^2	0.018	0.023	0.023	0.8	quasi-∥
		Kurtosis	3.56	3.50	3.23		
2016 Jan 11, 00:57:04–01:00:34	(9 R_e, −8 R_e)	χ^2	0.031	0.020	0.067	1.5	quasi-⊥
		Kurtosis	3.76	3.06	4.5		
2017 Jan 18, 00:45:54–00:49:42	(8 R_e, −5 R_e)	χ^2	0.020	0.067	0.113	1.8	quasi-∥
		Kurtosis	2.77	2.43	3.56		
2017 Jan 27, 08:02:03–08:08:03	(11 R_e, 6 R_e)	χ^2	0.04	0.09	0.02	2.1	quasi-∥
		Kurtosis	3.14	3.08	3.29		
2017 Dec 21, 06:41:55–07:03:51	(13 R_e, −1 R_e)	χ^2	0.085	0.022	0.019	2.1	quasi-∥
		Kurtosis	3.23	2.92	2.75		
2017 Dec 21, 07:21:54–07:48:01	(14 R_e, 0 R_e)	χ^2	0.012	0.094	0.045	1.9	quasi-∥
		Kurtosis	4.03	2.83	2.61		
2018 Apr 19, 05:08:04–05:41:51	(−3 R_e, −22 R_e)	χ^2	0.011	0.014	0.011	3.1	quasi-⊥
		Kurtosis	3.41	3.81	3.46		
2018 Apr 23, 07:50:14–08:33:41	(3 R_e, 18 R_e)	χ^2	0.019	0.035	0.027	1	quasi-⊥
		Kurtosis	3.54	3.47	3.73		
2018 Oct 27, 09:13:14–09:57:41	(−2 R_e, 24 R_e)	χ^2	0.017	0.010	0.029	2.5	quasi-∥
		Kurtosis	3.07	3.28	2.86		
2018 Nov 21, 16:10:14–16:55:31	(11 R_e, 13 R_e)	χ^2	0.010	0.049	0.009	0.9	quasi-⊥
		Kurtosis	3.84	3.75	2.92		
2018 Nov 29, 22:42:34–23:31:01	(11 R_e, 8 R_e)	χ^2	0.008	0.005	0.008	5	quasi-∥
		Kurtosis	3.04	2.90	3.10		
2018 Dec 5, 14:53:23—15:20:13	(12 R_e, 7 R_e)	χ^2	0.019	0.015	0.013	7.5	quasi-∥
		Kurtosis	3.39	2.95	2.82		
2019 Jan 11, 03:22:23–03:52:23	(12 R_e, 2 R_e)	χ^2	0.011	0.02	0.028	2.0	quasi-∥
		Kurtosis	3.52	2.56	2.94		
2019 Apr 5, 10:58:33–11:25:52	(12 R_e, −10 R_e)	χ^2	0.024	0.035	0.086	1.9	quasi-∥
		Kurtosis	2.66	2.69	2.63		

variances of the three components are close. Further, we check that each of these intervals exhibits a Kolmogorov "−5/3" spectrum, which is often considered an adequate indicator of well-developed turbulence. The collection of studied magnetosheath intervals are reported in Table B1, where we also report whether each interval is downstream of the quasi-parallel or quasi-perpendicular bow-shock region. The nature of turbulent fluctuations may be significantly different in the magnetosheath plasma downstream of the quasi-parallel and the quasi-perpendicular shock. The plasma downstream of the quasi-parallel shock is usually found to be more turbulent, relative to that of the quasi-perpendicular shock. The examined intervals include those corresponding to both kinds of shock and with a substantial variation in the normalized fluctuation amplitude $B_{rms}/\lvert\langle \boldsymbol{B}\rangle\rvert$.

From Table B1, we see that the kurtosis lies generally between 2.4 and 4.03, and the values of kurtosis and the fitness parameter χ^2 do not appear to change systematically from the quasi-parallel to the quasi-perpendicular shock. Although this is not a fully exhaustive sampling, it appears that turbulent magnetosheath fluctuations are often found in a near-Gaussian

state, as is common for fluctuations of the primitive variables in strong homogeneous turbulence (Batchelor 1951; Schumann & Patterson 1978).

Appendix C
Additional Supporting Analysis

We also perform the analyses presented in the main article, namely, Figures 2 and 3, for all the intervals listed in Table B1. Again, every interval is found to return a reasonably similar result (not shown here), with no systematic variation between quasi-parallel and quasi-perpendicular shocked plasma. The interval studied in the main article corresponds to the quasi-parallel shock. For demonstration, we show the corresponding figures produced for a long magnetosheath interval downstream of the quasi-perpendicular shock in Figure C1. Again, the agreement is satisfactory, and the scaling laws appear to hold, in general, for turbulent magnetosheath plasmas.

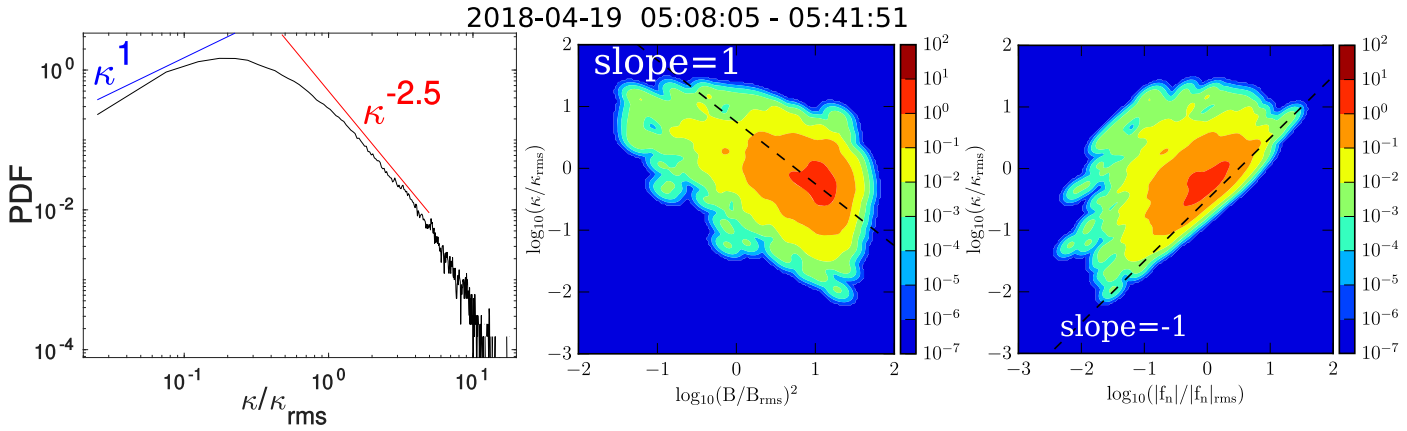

Figure C1. Magnetosheath plasma downstream of the quasi-perpendicular shock observed by MMS on 2018 April 19 (Table B1). Left: PDF of the magnetic field curvature κ normalized to its rms value κ_{rms}. Middle: joint PDF of curvature κ and the square of magnetic field magnitude B^2. Right: joint PDF of curvature κ and the magnitude of the force $|f_n|$ acting normal to the field lines.

ORCID iDs

Riddhi Bandyopadhyay https://orcid.org/0000-0002-6962-0959
William H. Matthaeus https://orcid.org/0000-0001-7224-6024
Alexandros Chasapis https://orcid.org/0000-0001-8478-5797
Tulasi N. Parashar https://orcid.org/0000-0003-0602-8381
Christopher T. Russell https://orcid.org/0000-0003-1639-8298
Robert J. Strangeway https://orcid.org/0000-0001-9839-1828
Roy B. Torbert https://orcid.org/0000-0001-7188-8690
Barbara L. Giles https://orcid.org/0000-0001-8054-825X
Daniel J. Gershman https://orcid.org/0000-0003-1304-4769
Craig J. Pollock https://orcid.org/0000-0001-9228-6605
Thomas E. Moore https://orcid.org/0000-0002-3150-1137
James L. Burch https://orcid.org/0000-0003-0452-8403

References

Akhavan-Tafti, M., Slavin, J. A., Sun, W. J., Le, G., & Gershman, D. J. 2019, GeoRL, 46, 12654
Batchelor, G. K. 1951, PCPS, 47, 359
Boozer, A. H. 2005, RvMP, 76, 1071
Burch, J. L., Moore, T. E., Torbert, R. B., & Giles, B. L. 2016, SSRv, 199, 5
Dahlin, J. T., Drake, J. F., & Swisdak, M. 2014, PhPl, 21, 092304
Dobrott, D., Nelson, D. B., Greene, J. M., et al. 1977, PhRvL, 39, 943
Dunlop, M., Southwood, D., Glassmeier, K.-H., & Neubauer, F. 1988, AdSpR, 8, 273
Fang, Z., Wang, J., Liu, B., & Gong, W. 2012, in Double Pareto Lognormal Distributions in Complex Networks, ed. M. T. Thai & P. M. Pardalos (Boston, MA: Springer US), 55
Franz, M., & Harper, D. 2002, P&SS, 50, 217
Gershman, D. J., Vinas, A. F., Dorelli, J. C., et al. 2018, PhPl, 25, 022303
Guo, F., Liu, Y.-H., Daughton, W., & Li, H. 2015, ApJ, 806, 167
Hameiri, E., Laurence, P., & Mond, M. 1991, JGR, 96, 1513
Hoshino, M., Mukai, T., Terasawa, T., & Shinohara, I. 2001, JGR, 106, 25979
Jokipii, J. R. 1982, ApJ, 255, 716
Matthaeus, W. H., Wan, M., Servidio, S., et al. 2015, RSPTA, 373, 20140154
Mitzenmacher, M. 2004, Internet Mathematics, 1, 226
Monin, A. S., & Yaglom, A. M. 1971, Statistical Fluid Mechanics, Vol. 1 (Cambridge, MAss: MIT Press)
Padhye, N., Smith, C. W., & Matthaeus, W. H. 2001, JGRA, 106, 18635
Parashar, T. N., Chasapis, A., Bandyopadhyay, R., et al. 2018, PhRvL, 121, 265101
Paschmann, G., & Daly, P. W. 1998, Analysis Methods for Multi-Spacecraft Data, http://hdl.handle.net/11858/00-001M-0000-0014-D93A-D
Pesses, M. E., Eichler, D., & Jokipii, J. R. 1981, ApJL, 246, L85
Petschek, H. E. 1964, in Physics of Solar Flares, ed. W. N. Hess (Washington, DC: NASA SP-50), 425
Pollock, C., Moore, T., Jacques, A., et al. 2016, SSRv, 199, 331
Reed, W. J. 2001, Economics Letters, 74, 15
Reed, W. J., & Hughes, B. D. 2002, PhRvE, 66, 067103
Reed, W. J., & Jorgensen, M. 2004, Communications in Statistics—Theory and Methods, 33, 1733
Rong, Z. J., Wan, W. X., Shen, C., et al. 2011, JGRA, 116, A09218
Russell, C. T., Anderson, B. J., Baumjohann, W., et al. 2016, SSRv, 199, 189
Schumann, U., & Patterson, G. S. 1978, JFM, 88, 685
Shen, C., Li, X., Dunlop, M., et al. 2003, JGRA, 108, 1168
Shen, C., Li, X., Dunlop, M., et al. 2007, JGRA, 112, A06211
Slavin, J. A., Lepping, R. P., Gjerloev, J., et al. 2003, JGRA, 108, 1015
Stawarz, J. E., Eastwood, J. P., Phan, T. D., et al. 2019, ApJL, 877, L37
Sun, W. J., Slavin, J. A., Tian, A. M., et al. 2019, GeoRL, 46, 6168
Whang, Y. C. 1977, Solar Phys., 53, 507
Yang, Y., Wan, M., Matthaeus, W. H., et al. 2019, PhPl, 26, 072306